Moiré pattern assisted commensuration resonance in disordered twisted bilayer graphene

Zhe Hou [1,2] Ya-Yun Hu,[1,*] and Guang-Wen Yang[1,3]
[1]*Zhejiang Lab, Hangzhou 311100, People's Republic of China*
[2]*School of Physics and Technology, Nanjing Normal University, Nanjing 210023, China*
[3]*Department of Computer Science and Technology, Tsinghua University, Haidian District, Beijing 100084, People's Republic of China*

(Received 2 August 2023; revised 26 December 2023; accepted 17 January 2024; published 13 February 2024)

We investigate the mesoscopic transport through a twisted bilayer graphene (TBG) consisting of a clean graphene nanoribbon on the bottom and a disordered graphene disk on the top. We show that, with strong top-layer disorder, the transmission through such a device shows a sequence of resonant peaks with respect to the rotation angle θ, where at the resonant angles θ_c the disk region contains one giant hexagonal moiré supercell. A further investigation shows that the value of θ_c shows negligible dependence on the disorder strength, the Fermi energy, and the shape distortion, indicating the resonance is a robust commensuration feature of the moiré supercell. We explain this commensuration resonance based on the bound states formed inside TBG disk as a result of the nonuniform interlayer coupling, with their average local density of states dominating at the AA stacking region while minimizing at the AB/BA stacking regions. By increasing the interlayer distance, the peak becomes less pronounced which further confirms the role of interlayer coupling. The results presented here suggest a new mechanism to tune the quantum transport signal through the twist angle in disordered moiré systems.

DOI: 10.1103/PhysRevB.109.085412

I. INTRODUCTION

Twisted bilayer graphene (TBG), a graphene bilayer stacked with a rotation angle θ, has received tremendous research interest since the first experimental observations on superconductor and Mott insulator phases [1,2] at the first magic angle $\theta \approx 1.1^\circ$. The interesting strong correlation phenomenon existing in a simple carbon-based two-dimensional (2D) structure, provides an exciting platform for investigating strong correlation physics [3,4], and new experimental techniques in exploring the mechanism of high-T_c superconductors [5–11]. A small twist angle generates a giant moiré pattern with the moiré periodicity scaling inversely with θ, and simultaneously a reduced mini-Brillouin zone. The Fermi velocity at the Dirac point is renormalized by the twist angle and approaches zero at the magic angles [12–14], which induces flat bands [15] where strong electron-electron correlation dominates and many other interesting macroscopic quantum phases arise [3,4], such as ferromagnetism [16–19], and quantum anomalous Hall insulator phases [20–22]. Up to now, the twisted structure has been extended to twisted trilayer [23–28] or twisted bilayer-bilayer graphene [29,30], and other 2D Van der Waals layered materials [31–33] where interesting results have also been reported.

Till now, most recent investigations in TBG have been focusing on the strong correlation physics near the magic angle where translationally invariant morié supercells are formed in the TBG bulk. However, for applications of twisting techniques to design novel nanodevices, the influence of the edge, the shape distortion as well as the disorder effect that inevitably exist during the fabrication should also be considered. These factors not only break the translational symmetry but also make the exact commensurate angles invalid in finite-size samples. Existing works have investigated the quantum transport behavior in mesoscopic TBG devices in view of its unique electronic properties [34–42]. For example, the interplay between the zigzag edge and the TBG quantum dot (QD) can strongly modify the zero-energy density of states (DOSs) and the low-energy conductance [37–39]. Besides, it is found that the twisting axis can significantly influence the oscillating amplitude of conductance with respect to the twist angle, a phenomenon that is appreciably evident only in small devices while gradually disappears in large systems [40]. In addition to pristine TBG, the role of disorder or dephasing in quantum transport has also been examined, with a particular focus on the commensurate angles in systems with moiré periodicity [43–48].

For small twist angles, mesoscopic TBG samples host the natural QD properties that are formed by the moiré pattern as a result of the nonuniform interlayer coupling in which the wave functions near the flat band are mostly localized at the AA stacking region with their values minimizing at the AB/BA stacking regions [14,49–55]. Besides, this nonuniform interlayer coupling also generates a noncrystal system for an arbitrary twist angle, where quantum interference induces strong conductance fluctuation as a result of the noncrystal structure. The conductance fluctuation also arises from the finite-size effect when the system shrinks into a mesoscopic scale. However, this fluctuation can be eliminated by disorder or dephasing effect. So to investigate the quantum transport behavior through a mesoscopic TBG system, especially in

*yyhu@zhejianglab.edu.cn

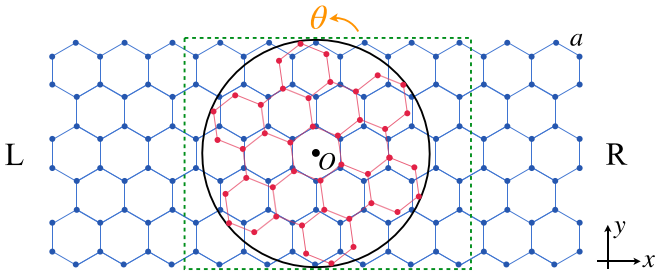

FIG. 1. Schematic diagram of a two-terminal TBG transport system. Here the top-layer graphene is in a disk shape (shown within the black circle) and is twisted with an angle θ relative to the origin O (set as the center of the bottom layer) anticlockwise. The transport system can be divided into three parts: left (right) lead L (R) and the central region (labeled by the green dashed rectangle). The width of the bottom nanoribbon can be represented by the number of carbon atoms N along any vertical line crossing with the atoms in the bottom layer. In this diagram, $N = 6$ is shown.

searching for the universal behavior of the angle dependence of conductance when both the atomic structure and the boundary of TBG change, it is important to impose one of the two effects.

In this paper, we consider a mesoscopic TBG system (Fig. 1) where the bottom layer is a pristine graphene nanoribbon while the top one is a disordered graphene disk with its center aligned with the bottom hexagon. The reason of keeping the bottom layer clean is to avoid localization effect when the applied disorder is strong, so that a high transmission through the TBG is guaranteed. We then rotate the top layer disk by an angle θ, and investigate the transport properties through such a device. We find that, when the disorder strength exceeds a critical value the average transmission T_A through the TBG device shows a global increase with the rotation angle θ for $\theta < 30^\circ$, and remarkably, exhibits a sequence of resonant peaks at several angles θ_c. By plotting the moiré structure of the TBG at the resonant angles, we find that the resonance happens when the top disk encompasses one gaint hexagonal moiré supercell which can be further decomposed into $3n^2 - 3n + 1$ AA stacking spots (we will call them the moiré unit cells below) for the nth peak. We then consider the parameter dependence of the resonant peaks by varying the disorder strength and range, the Fermi energy, the armchair/zigzag edge, and the shape of the TBG region, and find that the positions of the resonant angles are quite robust against all these changes. We thus dub this phenomenon a commensuration resonance. Finally, we investigate the scaling behavior of the resonant angles θ_c with respect to the radius R of the top disk and find the relation: $R \propto 1/(\sin\theta_c/2)$, in good agreement with the theoretically estimated size of the giant moiré supercell. The results presented here provide a new perspective into the role of disorder in TBG systems and suggest the twisting angle as a tuning knob for quantum transport in disordered moiré systems on a mesoscopic scale.

This paper is organized as follows. In Sec. II, we introduce the model and Hamiltonian of our setup. In Sec. III, we show the transport results of the TBG system with a circular boundary with and without the top-layer disorder. We also give interpretations on the resonant transmission based on the moiré patterns of the TBG. In Sec. IV, we change the shape of the central TBG region and show the robustness of the conductance peaks accompanied by the formation of moiré patterns. In Sec. V, we discuss the scaling relation between the size of the TBG region and the resonant angle θ_c. In Sec. VI, we discuss the disappearance of the resonant phenomenon in the presence of both-layer disorder. Finally in Sec. VII, we give some discussions and draw conclusions. Some details and other supplementary calculations are given in Appendices.

II. MODEL AND METHODS

The transport system we investigate is shown in Fig. 1. Here the origin O is set as the center of the hexagon on the bottom layer. The primitive vectors of the bottom monolayer graphene are $\boldsymbol{a}_{1(2)} = a(\frac{\sqrt{3}}{2}, \pm\frac{3}{2}, 0)$, with a the carbon-carbon atomic distance. The width W of the bottom nanoribbon can be denoted by the number of atoms N along any vertical line crossing with them, and has the relation: $W = (3N/2 - 1)a$. Here we consider the top layer confined within a disk geometry with a radius $R = W/2$, which can be obtained by physical etching or chemical synthesis [56], and is rotated anticlockwise with an angle θ with respect to O. A zigzag edge of the bottom nanoribbon has been chosen. The interlayer distance is denoted as d. At zero rotation angle $\theta = 0$, the top and bottom layer is in an AA-stacking style where the carbon atoms on the top layer are exactly aligned with the bottom ones. The advantage of using a disk geometry is that the overlapping area between the two layers is kept invariant upon rotation [40,41].

We only consider the p_z orbital of each carbon atom which consists of two types of hopping: $pp\pi$ and $pp\sigma$. The tight-binding Hamiltonian describing the TBG system can be written as [49,50]

$$H = \sum_i |i\rangle \varepsilon_i \langle i| + \sum_{\langle i,j\rangle} |i\rangle t_{ij} \langle j|, \tag{1}$$

where $|i\rangle$ is the p_z orbital localized at atom i with position $\boldsymbol{r}_i$, ε_i is the on-site energy, and $\langle i, j\rangle$ denotes the two neighboring carbon atoms with positions $\boldsymbol{r}_i$, $\boldsymbol{r}_j$ $(i \neq j)$. The coupling element t_{ij} has the following position dependent relation [57]:

$$t_{ij} = [\chi^2 V_{pp\sigma}(r_{ij}) + (1 - \chi^2) V_{pp\pi}(r_{ij})] \cdot \Theta\big(2\sqrt{3}a - \sqrt{r_{ij}^2 - |\boldsymbol{r}_{ij} \cdot \hat{\mathbf{e}}_z|^2}\big). \tag{2}$$

Here χ is the direction cosine of $\boldsymbol{r}_{ij} \equiv \boldsymbol{r}_j - \boldsymbol{r}_i$ along the z direction, which can be expressed as $\chi = \frac{\boldsymbol{r}_{ij} \cdot \hat{\mathbf{e}}_z}{r_{ij}}$ with $r_{ij} = |\boldsymbol{r}_{ij}|$ the distance between two atoms and $\hat{\mathbf{e}}_z$ the unit vector along z direction. The $pp\sigma$ and $pp\pi$ types of coupling strength in Eq. (2) are determined by the Slater-Koster relation [57]: $V_{pp\sigma}(r_{ij}) = \gamma_1 e^{(a_I - r_{ij})q_\sigma/a_I}$, and $V_{pp\pi}(r_{ij}) = -\gamma_0 e^{(a - r_{ij})q_\pi/a}$. In the following calculations, we set the intralayer carbon-carbon atomic distance $a = 1.418$ Å, and the interlayer distance $d = a_I$ with $a_I = 3.349$ Å. The interlayer distance will be fixed unless otherwise stated. The coupling energies are set to $\gamma_0 = 2.7$ eV and $\gamma_1 = 0.48$ eV. The exponential decay coefficients regarding the distance r_{ij} are set to be the same for $V_{pp\pi}$ and

$V_{pp\sigma}$: $q_\pi/a = q_\sigma/a_I = 2.218$ Å^{-1}. These parameters are most commonly used in the literature [49–51,58] and fit the DFT calculations well. Since the hopping strength decays exponentially with the distance and approaches the order of 1meV after the in-plane distance $\sqrt{r_{ij}^2 - |\boldsymbol{r}_{ij}\cdot\hat{\mathbf{e}}_z|^2} > 2\sqrt{3}a$, we set $2\sqrt{3}a$ as the hopping boundary in Eq. (2). As a result of this long-range hopping, the Dirac point of monolayer graphene is lifted approximately to $E_D = 0.8$ eV.

In designing the quantum transport device, we divide our system into three parts in Fig. 1: lead L (R), which are semi-infinitely long monolayer graphene nanoribbons, and the central bilayer region as labeled by the green dashed rectangle. The disorder can exist only on the top layer, or on both layers within the overlapping region, and is incorporated into the tight-binding Hamiltonian by adding a random electrostatic potential U_i to the on-site term: $\varepsilon_i = \varepsilon_0 + U_i$, where ε_0 is the uniform on-site energy which is set to zero throughout the paper. In the main part of our paper, we show the calculations with only-top layer disorder, which can be experimentally realized by doping or adhering adatoms on the top layer graphene taking advantage of the bilayer structure. The disorder potential has a uniform distribution within $[-V_d/2, V_d/2]$ with V_d characterizing the top-layer disorder strength. The calculations with both-layer disorder will be only shown in Sec. VI.

In calculating the conductance through the TBG region we resort to the nonequilibrium Green's function method. The surface Green's functions $\mathbf{g}^r_{s,L(R)}(E)$ for the lead L(R) with E the incident energy (defined relative to the Dirac point $E_D = 0.8$ eV) is firstly calculated using the recursive method [59,60]. The self-energy of the lead L(R) is calculated as $\mathbf{\Sigma}^r_{L(R)}(E) = \mathbf{H}_{C,L(R)}\mathbf{g}^r_{s,L(R)}(E)\mathbf{H}^\dagger_{C,L(R)}$ with $\mathbf{H}_{C,L(R)}$ the coupling matrix between the central region and lead L(R). The retarded Green's function of the central region is then calculated to be $\mathbf{G}^r_C(E) = [(E + i\eta)\mathbf{I} - \mathbf{H}_C - \mathbf{\Sigma}^r_L - \mathbf{\Sigma}^r_R]^{-1}$, where η is an infinitesmall positive number [61]. The Green's function $\mathbf{G}^r_C(E)$ can be numerically calculated iteratively (more details can be found in Appendix A), and the final transmission coefficient $T(E)$ through the TBG region is calculated to be [62,63]

$$T(E) = \mathrm{Tr}\left[\mathbf{\Gamma}_L\mathbf{G}^r_C\mathbf{\Gamma}_R\mathbf{G}^a_C\right], \tag{3}$$

where $\mathbf{\Gamma}_{L(R)}(E) \equiv i[\mathbf{\Sigma}^r_{L(R)} - (\mathbf{\Sigma}^r_{L(R)})^\dagger]$ is the linewidth function for lead L(R), and $\mathbf{G}^a_C(E) = [\mathbf{G}^r_C(E)]^\dagger$ is the advanced Green's function of the central region. We consider the transport happens at zero temperature, so the differential conductance at Fermi energy E_F is calculated to be: $G(E_F) = \frac{2e^2}{h}T(E_F)$ (here the factor 2 accounts for spin).

III. TRANSPORT RESULTS FOR A TBG WITH CIRCULAR BOUNDARY

The TBG system has a periodicity of 60° with respect to the rotation angle θ (see Appendix B), and as a result of the mirror symmetry along the x axis, it suffices to only consider the rotation range within $[0, 30°]$. In Fig. 2(a), we first plot the band structure of the bottom graphene nanoribbon with $N = 50$. Due to the finite width along the y direction, a few subbands are formed. Two Dirac points can be seen at $E = 0$

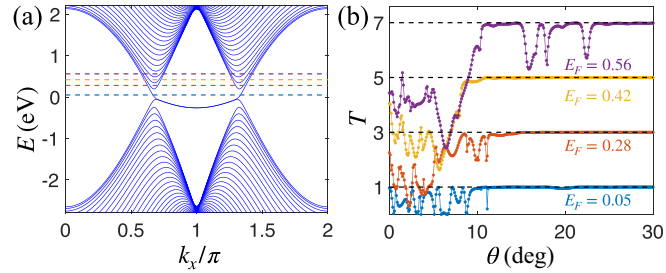

FIG. 2. (a) Band structure of the bottom graphene nanoribbon with $N = 50$ with long-range hopping. The Fermi energy E_F of the transport system is shown with the dashed lines with values (counted from bottom to top): $E_F = 0.05,\ 0.28,\ 0.42$, and 0.56 eV (defined relative to the Dirac point of graphene $E_D = 0.8$ eV), which correspond to channel numbers 1, 3, 5, and 7, respectively. (b) The angle dependence of the transmission coefficient T without disorder at different E_F. Here the interlayer distance $d = a_I$. The black dashed lines label the number of incident channels from the leads.

and there are two branches of topologically nontrivial bands connecting the two Dirac points as a result of the zigzag edge of the nanoribbon [64]. As a result of the long-range hopping the particle-hole symmetry has been broken [12,53]. In Fig. 2(b), we show the transmission coefficient T through the TBG region as a function of θ. At zero disorder, the TBG in the central region of the transport device works as a chaotic system where the phase interference occurs randomly by slightly varying the rotation angle. As a result, for $\theta < 11°$ a strong fluctuation in the transmission curve can be seen in Fig. 2(b), consistent with Ref. [65] where incommensurate twist angle plays the role of an effective disorder. The strong fluctuation for θ close to zero at $E_F = 0.05$ eV where the mode can only be scattered from one valley to another, indicates a strong intervalley scattering due to the sharp circular boundary. At $\theta > 11°$, the TBG system goes into the decoupling regime [45], where the top layer has almost zero influence on the electron transport through the bottom layer, so the transmission plateau with its value equal to the number of incident modes can be seen. The appearance of dips on the plateau for higher Fermi level $E_F = 0.56$ eV is reminiscent of the antiresonance in a ballistic conductor by coupling with a quantum dot [66]. For $\theta = 30°$, a quasicrystal structure is formed in the TBG [67–69], where the interlayer coupling is weak, and the double monolayer graphene are effectively decoupled. This explains the perfect transmission for θ around 30°.

In Fig. 3(a), we show the average transmission coefficients T_A in the presence of top-layer disorder. For weak disorder case ($V_d \leqslant 2$ eV), the fluctuation in the transmission curve still exists but becomes smaller as a result of the ensemble average. However, for stronger disorder ($V_d \geqslant 3$ eV), the fluctuation has been smeared out and all the transmission curves become smooth. Besides, an overall increase of T_A can be seen as increasing θ, indicating that the effective interlayer coupling becomes weaker with increasing the rotating angle, consistent with Refs. [70,71]. The transmission curves saturate in the decoupling limit of $\theta = 30°$ with the saturating values decreasing with increasing the disorder strength, indicating that the top-layer disordered graphene can still influence the

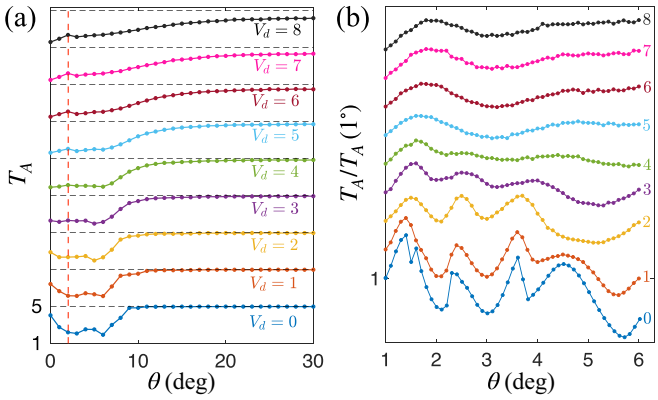

FIG. 3. (a) Average transmission coefficient T_A as a function of the rotation angle θ for different top-layer disorder strength V_d. Here the Fermi energy is $E_F = 0.42\,\text{eV}$ which crosses five conducting channels in the leads. The red dashed line denotes the angle at $\theta = 2°$. The horizontal dashed lines denote the same scale range of [1, 5]. (b) Normalized transmission coefficients $T_A/T_A(1°)$ within the range $[1°, 6°]$ with denser plots. Here each line with increased disorder strength has been lifted with a value of 0.2. The number on each curve is the disorder strength (shown with the same color). Here we choose the width of the bottom layer $N = 50$, the radius of the top disk $R = W/2$, and the interlayer distance $d = a_I$. The energy-unit is in eV and has been omitted here. The disorder exists only on the top layer and each disordered curve was averaged for 1000 times (a good convergence can be seen in Appendix C).

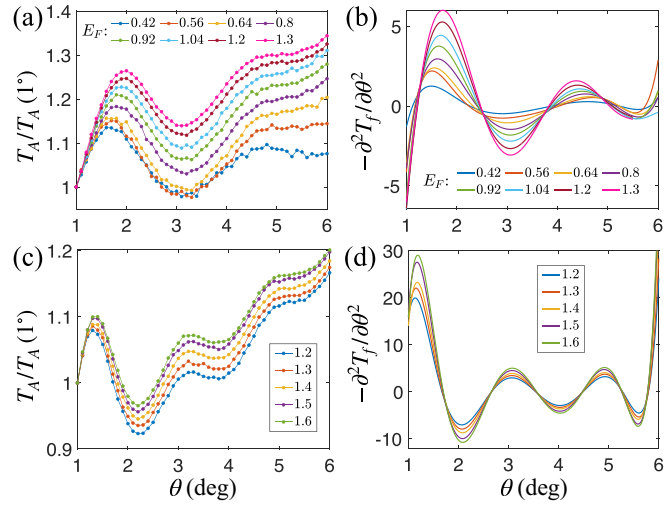

FIG. 4. [(a) and (c)] The average transmission T_A [normalized by $T_A(1°)$] as a function of rotation angle θ for $N = 50$ and $N = 70$, respectively. Here the top-layer disorder strength is fixed to $V_d = 5\,\text{eV}$. The Fermi energy E_F in each subfigure is tuned. [(b) and (d)] The second derivative of the average conductance $-\partial^2 T_f/\partial\theta^2$ obtained from the smooth polynomial fitting T_f for (a) and (c), respectively. Other parameters are the same as Fig. 3.

quantum transport through the bottom one in the decoupling regime.

At $\theta \approx 2°$ [see the red dashed line in Fig. 3(a)], we notice a remarkable transmission peak for all transmission curves with $V_d \geqslant 3\,\text{eV}$, implying the existence of a resonant state in the central TBG region. To make a detailed investigation on the resonant peak, we zoom in the curves for θ within $[1°, 6°]$ and consider a denser plotting in Fig. 3(b). A renormalization has been made for each disordered curve by dividing its value at $\theta = 1°$. We note that the resonant peaks become clearer after $V_d \geqslant 5\,\text{eV}$ in Fig. 3(b). In this case, a calculation on the localization length [72] at $V_d = 5\,\text{eV}$, giving the value $\lambda_L \approx 35.5$ nm, means that the transport through the top layer is close to the localization regime (the diameter of the top disk is 10.5 nm).

In Fig. 4, we change the Fermi energy E_F and show the energy dependence of the resonant peaks. In Fig. 4(a), we consider the width of the bottom nanoribbon $N = 50$ and choose the Fermi energy ranging from 0.42 to 1.3 eV. The disorder strength is fixed to $V_d = 5\,\text{eV}$. We note that for each disordered curve, a pronounced peak can be seen at $\theta \approx 2°$. The position of the first resonant angle θ_{c1} has a slight rightward shift when the energy increases due to the overall increase of T_A. The origin of the shift can be attributed to the background E_F dependence of the transmission that is related to system details. For certain E_F, we may expand the θ dependence of the disorder-averaged transmission around the resonance angle θ_c to the second order: $T(\theta) = p_0(E_F) + p_1(E_F)(\theta - \theta_c) - p_2(E_F)(\theta - \theta_c)^2$, where $p_{0,1,2} > 0$ are parameters that depend on E_F. The position of the peaks can be found by finding the extreme points of $T(\theta)$: $\theta_{\text{peak}} = \theta_c + \frac{p_1(E_F)}{2p_2(E_F)}$, which is expected to move rightward if $p_1(E_F)/p_2(E_F)$ increases with the increasing of E_F and vice versa. We ascribe the observed deviation of the resonant peaks to the E_F dependence of the p parameters. Besides, a second resonant peak can be observed. The position of the second resonant peak also moves as varying E_F and shows a leftward moving. To show the resonant peaks more clearly, we use the polynomial curving fitting for the average transmission T_A to get T_f, and plot the second derivative $-\frac{\partial^2 T_f}{\partial\theta^2}$ in Fig. 4(b). We note that the resonant peaks become more prominent in this case, and the first resonant angle θ_{c1} comes into an almost fixed value when E_F reaches 1.3 eV.

In Figs. 4(c) and 4(d), we also plot the similar transmission curves for $N = 70$. Here the Fermi energy is tuned from 1.2 to 1.6 eV so that more incident modes from the leads are included. Except for the first two resonant peaks, a third one which is in the middle of the first two can be observed. After performing the second derivative, we obtain three prominent resonant peaks in each curve in Fig. 4(d). The positions of these peaks are almost fixed as varying the Fermi energy E_F since the overall increase of T_A with respect to θ has been eliminated by the second derivative.

The resonant tunneling through the disordered TBG system, which is very robust against the disorder strength V_d and Fermi energy E_F, implies a pure commensuration resonance phenomenon that has deep connections with the geometry of the moiré pattern in TBG. To see this, we read out the resonant angles $\theta_{c1} = 1.71°, \theta_{c2} = 4.4°$ from the curve of $E_F = 1.2\,\text{eV}$, $V_d = 5\,\text{eV}$, and $N = 50$ [73] in Fig. 4(b), and plot the moiré pattern of the TBG in Figs. 5(a) and 5(b). We note that for the first resonant angle θ_{c1}, a whole moiré supercell is perfectly encoded inside the central circle, with the boundary of the disk crossing the AB/BA stacking regions. For the second resonant angle θ_{c2}, a denser moiré pattern can be seen in Fig. 5(b).

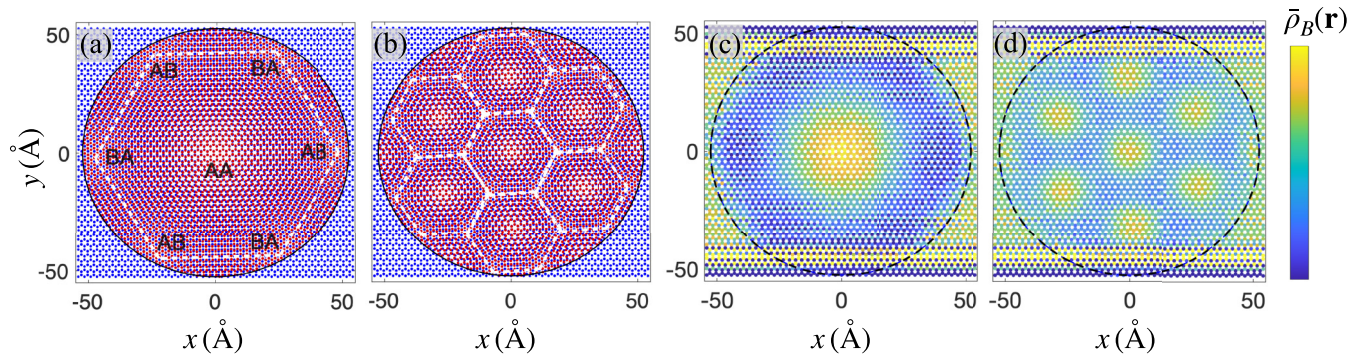

FIG. 5. The moiré pattern of the TBG system at the first resonant angle $\theta_{c1} = 1.71^\circ$ in (a) and the second resonant angle $\theta_{c2} = 4.4^\circ$ in (b). Here the width of the bottom nanoribbon is $N = 50$. The resonant angles θ_c were read out from the second derivative of the conductance curves at $E_F = 1.2$ eV in Fig. 4(b). The black circles denote the boundary of the top disk. The white dashed lines are guidelines for the moiré unit cells. [(c) and (d)] The averaged local DOSs $\bar{\rho}_B(\mathbf{r})$ of the bottom nanoribbon in the central region with the same rotation angles as (a) and (b), respectively. Here we set $d = a_I$ and $V_d = 5$ eV. The averaged DOSs are summed within the energy window [0.9, 1.5] eV. The disorder is averaged for 50 times.

In this case, the central disk also contains a giant hexagonal moiré supercell which can be decomposed into seven moiré unit cells (as can be seen by the white dashed lines) centered at the AA stacking region. The boundary of the disk also crosses exactly the AB/BA stacking regions which are just the outer boundary of the giant hexagonal moiré supercell.

To explain the resonant tunneling, we plot the ensemble-averaged local DOSs $\bar{\rho}_B(\boldsymbol{r}) \equiv \langle \int_{E_1}^{E_2} \rho_B(E, \boldsymbol{r}) \mathrm{d}E \rangle$ in the bottom layer, where $\rho_B(E, \boldsymbol{r})$ is the local DOSs at position $\boldsymbol{r}$ on the bottom layer at energy E, $[E_1, E_2]$ is the energy integral window, and $\langle\rangle$ is the ensemble average. In Figs. 5(c) and 5(d), we plot the distribution of $\bar{\rho}_B(\boldsymbol{r})$ at rotation angles $\theta_{c1,2}$. As expected, the local DOSs are mainly located at AA-stacking regions, and minimizes at AB/BA-stacking regions, indicating the existence of the resonant states as a result of the nonuniform interlayer coupling. As expected, the bright spots in the local DOSs have a perfect agreement with the moiré patterns in Figs. 5(a) and 5(b), working as a fingerprint of the moiré structure for the TBG. The presence of high local DOSs on the edges contributes to a global enhancement to the transport in the background of the resonant tunneling. The resonant states are consistent with previous analysis based on the QD property of TBG [14,49–55], which mainly considers this localization property in bulk TBG. Here in our work the TBG region is geometrically more like an isolated QD, but the distribution of the averaged local DOSs still agrees well with the localization property in bulk TBG. The isolated QD structure is similar to Ref. [58] where a circular TBG QD defined by an infinite-mass potential is investigated, and the distribution of the local DOSs shows good consistency with each other. The occurrence of the resonant peaks can be understood by making an analogy with the cotunneling of a mesoscopic QD: in normal QD systems, once the energy of the incident electrons matches the bound level inside the quantum dot, electrons can transmit through the QD with the probability one. Here in our work, once the TBG disk encompasses a whole giant hexagonal moiré supercell, the resonant tunneling happens by exhibiting a peak in the averaged transmission curves. The averaged local DOSs which are localized at AA regions and show minimum values at AB/BA regions, play the role of a channel mediating the resonant tunneling, in the similar way as the bound states in a normal QD.

The effect of the interlayer coupling on the quantum transport through the TBG region can be further validated by varying the interlayer distance d. Equation (2) enables us to increase(decrease) the strength of interlayer coupling by slightly decreasing(increasing) the interlayer distance d around its equilibrium point a_I. Experimentally this can be realized by using the hydrostatic pressure [74,75]. From Fig. 6(a), we see that when the interlayer distance is far ($d = 1.2a_I$), the top layer graphene has little effect on the bottom layer, and the resonant peaks can hardly be distinguished. As the interlayer distance is reduced, the resonant peaks become more prominent as a result of the enhanced interlayer coupling. Notably, the positions of the transmission peaks are insensitive to the finite change in d. In Fig. 6(b), we also plot the distribution of local DOSs $\bar{\rho}_B(\boldsymbol{r})$ for the bottom layer graphene with $d = 0.9a_I$ at the second resonant angle $\theta_{c2} = 4.4^\circ$. Compared with Fig. 5(d) with $d = a_I$, we see

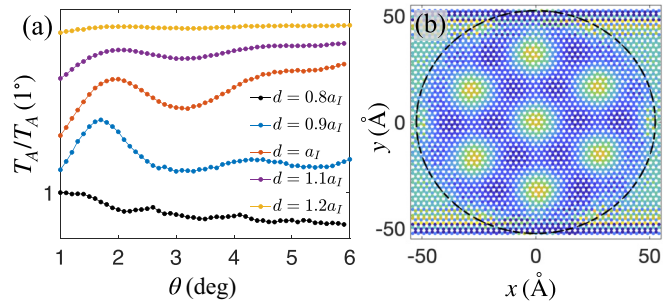

FIG. 6. (a) The average transmission T_A [normalized by $T_A(1^\circ)$] through the TBG disk with different interlayer distance d. Each curve with increasing d is shifted upward for clarity. The width of the nanoribbon is $N = 50$, the Fermi energy is $E_F = 1.2$ eV, the top-layer disorder strength $V_d = 5$ eV and each curve is averaged for 1000 times. (b) The averaged local DOSs $\bar{\rho}_B(\boldsymbol{r})$ on the bottom layer with interlayer distance $d = 0.9a_I$. The twist angle is chosen at the second resonant angle $\theta_{c2} = 4.4^\circ$. Other parameters are the same as Fig. 5(d).

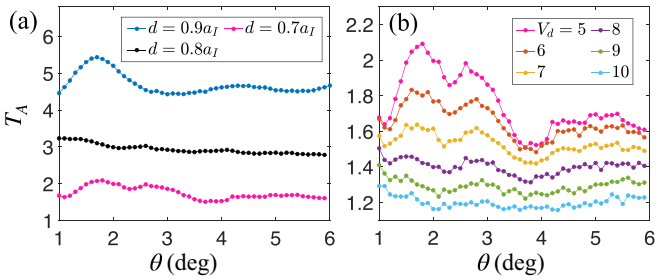

FIG. 7. (a) The average transmission T_A with different interlayer distance d. Here the top-layer disorder strength $V_d = 5\,\text{eV}$. (b) The average transmission T_A for $d = 0.7a_I$ as increasing the top-layer disorder strength V_d. Other parameters are the same as those of Fig. 6(a).

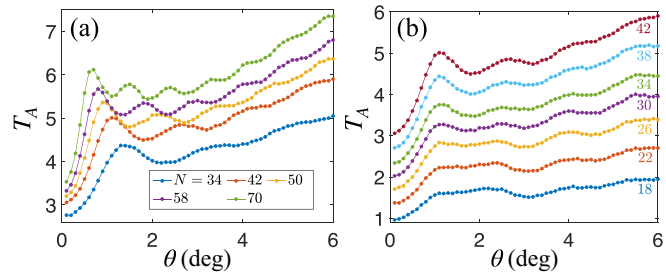

FIG. 9. The transport results of changing the shape of the central TBG region. (a) The average transmission T_A as a function of θ for different width of the bottom nanoribbon N by fixing the radius of the top disk $R = W$ and cutting off the unoverlapped area. (b) T_A as a function of θ by fixing the radius R of the top disk and changing the width N (see the numbers with the same colors as the curves) of the nanoribbon (also cutting off the unoverlapped area). Here we set $R = 62.5a$ (corresponding to $N = 84$ in the circular boundary case). In (a) and (b) we use the Fermi energy $E_F = 1.2\,\text{eV}$ and the top-layer disorder strength $V_d = 5\,\text{eV}$. Other parameters are the same as Fig. 3.

that the contrast of DOSs between the AA-stacking region and AB/BA-stacking regions becomes sharper, indicating the resonant states formed inside the moiré pattern become more localized, enhancing the resonant tunneling. However, when further decreasing the interlayer distance to $d = 0.8a_I$ and $0.7a_I$ [see Fig. 7(a)], we have found that the transmission peaks disappear due to the over-strong interlayer coupling. For $d = 0.7a_I$, the nearest interlayer hopping $V_{pp\sigma}(d)$ is around 4.46 eV, much larger than the nearest intralayer hopping. This strong interlayer coupling bends the band of the central TBG and pushes the p_z-orbital band away from the Fermi energy, and suppresses the transmission, as can be seen from the decreased transmission coefficient T_A in Fig. 7(a) in decreasing d. In Fig. 7(b), we try to weaken the dominance of the overstrong interlayer coupling on the transmission peaks by increasing the top-layer disorder strength. However, the results show that it only smears out the θ dependence and simultaneously reduces the transmission. No such resonant peaks as $d = 0.9a_I$ arise. So to observe the resonant phenomenon reported here one should keep the interlayer distance $0.8a_I < d < 1.2a_I$.

The moiré pattern at the commensuration resonant angles θ_c seems to exhibit the arithmetic sequence for the outer shell of the moiré supercell which has $6(n-1)$ moiré unit cells for the n-th resonant peak, which in total contains $S_n = 3n^2 - 3n + 1$ moiré unit cells inside the disk. To see this, we also plot the moiré patterns of $N = 70$ at the resonant angles $\theta_{c1} = 1.14^\circ$, $\theta_{c2} = 3.06^\circ$, and $\theta_{c3} = 4.93^\circ$ in Fig. 8. As expected, the first, second, and third resonant peaks yield 1, 7, and 19 moiré unit cells inside the circle in total.

IV. COMMENSURATION RESONANCE WITH SHAPE DISTORTION

To show that the resonant tunneling above is not a unique phenomenon as a result of the circular boundary in the TBG region, we here change the shape of the central overlapping region. This can be realized by increasing the radius R of the top disk or reducing the width N of the bottom nanoribbon, and then cutting off the remaining part outside the nanoribbon region. For example, an approximate rectangular TBG region can be obtained by setting a large R while fixing the nanoribbon width. In Fig. 9(a), we first fix $R = W$ and change N to study the average transmission as a function of θ. Here the Fermi energy is $E_F = 1.2\,\text{eV}$, and the top-layer disorder strength $V_d = 5\,\text{eV}$. We see that, even though the shape of the central TBG is distorted, the sequence of resonant peaks

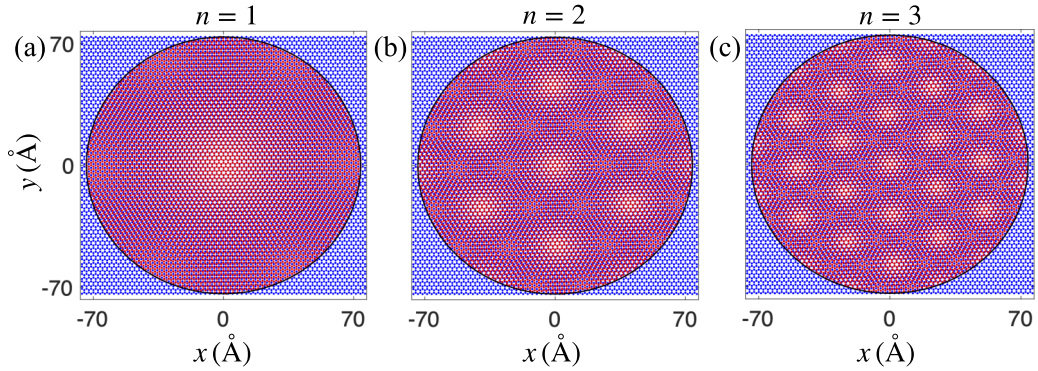

FIG. 8. The moiré pattern for the first resonant angle $\theta_{c1} = 1.14^\circ$ in (a), the second resonant angle $\theta_{c2} = 3.06^\circ$ in (b), and the third resonant angle $\theta_{c3} = 4.93^\circ$ in (c). Here the width of the bottom nanoribbon is $N = 70$. The critical angles θ_c were read out from the second derivative of the conductance curves at $E_F = 1.2\,\text{eV}$ in Fig. 4(d). The black circles denote the boundaries of the top disk.

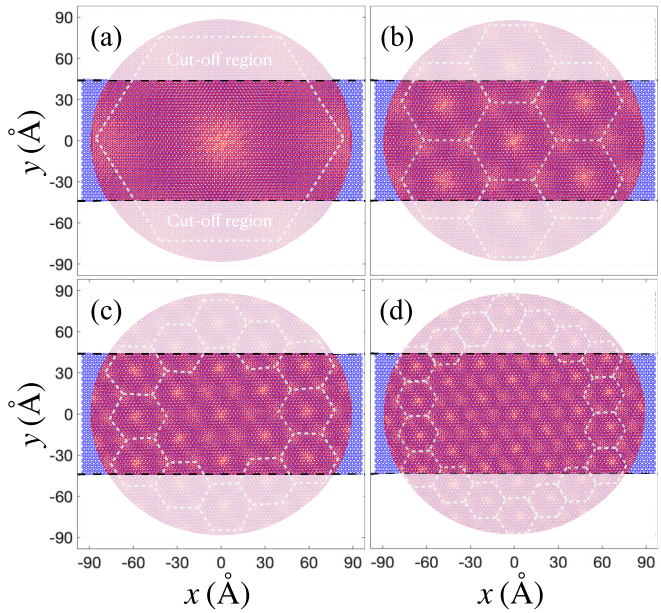

FIG. 10. [(a)–(d)] Moiré pattern for the TBG disk with $R = 62.5a$ at the resonant angles: $\theta_{c1} = 1^\circ$, $\theta_{c2} = 2.55^\circ$, $\theta_{c3} = 4.2^\circ$, and $\theta_{c4} = 5.6^\circ$, respectively, corresponding to $N = 42$ in Fig. 9(b). Here the transport device only exists in the central region between the two black dashed lines. Other blurred areas are cut-off regions not included in the transport device, and are plotted only to show the whole moiré supercell for clarity. The white dashed hexagons are guidelines for the moiré unit cells for the outer shell of the giant hexagonal supercell.

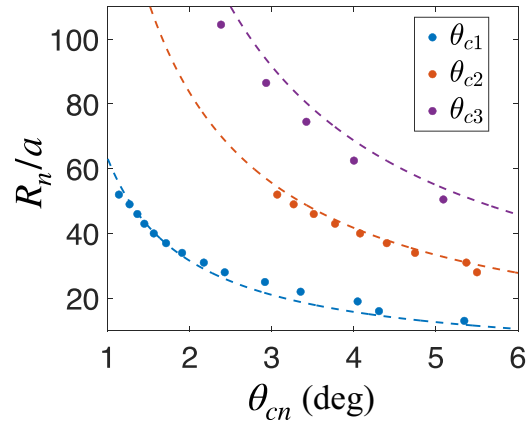

FIG. 11. Scaling relation of the radius of the top layer disk R with respect to the resonant angles θ_c for the first, second and third resonant peaks. Here the Fermi energy is $E_F = 1.2\,\text{eV}$, and the disorder strength is $V_d = 5\,\text{eV}$. Each dot was obtained by reading from the second derivative of the polynomial fitted curves from the average conductance curves. The dashed lines are the theoretically estimated scaling relation between R_n and θ_{cn}. Here a modification factor $\zeta = 1.1$ has been used to account for the overfilling of the moiré pattern inside the top disk.

can still be observed. Besides, the resonant angles at the nth peak become smaller as increasing N. These behaviors are similar to those in Fig. 4, indicating the same resonant phenomenon arising from the formation of the moiré pattern. In addition, higher resonant peaks like the fourth and fifth can also be seen albeit less obvious than the first three ones. To see other shapes of the TBG region, we fix the radius of the top disk by setting $R = 62.5a$ (corresponding to $N = 84$ in the circular boundary case) and decrease the width N of the nanoribbon from 42 to 18, where for the last case the TBG region becomes a quasi-one-dimensional nanochain. The Fermi energy is also chosen to be $E_F = 1.2\,\text{eV}$ and the average transmission coefficient T_A can be seen in Fig. 9(b). We see that for small width of the nanoribbon ($N = 18$ and 22), the resonant peaks can hardly be distinguished as a result of the incomplete moiré supercell within the TBG region. However, for $N \geqslant 26$, four almost equally distributed resonant peaks can be seen with their positions almost fixed as varying N (especially for the first peak which is pinned at $\theta = 1.1^\circ$). Besides, the resonant peaks become more pronounced as N increases.

In Fig. 10, we show the moiré patterns at the resonant angles: $\theta_{c1} = 1^\circ$, $\theta_{c2} = 2.55^\circ$, $\theta_{c3} = 4.2^\circ$, and $\theta_{c4} = 5.6^\circ$ for the resonant peaks of $N = 42$ in Fig. 9(b). Here we emphasize that the top layer graphene only exists in the overlapping region between the disk and the bottom nanoribbon (shown in the central region between the two black dashed lines in Fig. 10). The extended blurred regions are only shown for clarity. We find that these results are the same as those in Figs. 5 and 8. We label the moiré unit cells at the outer shell of the giant hexagonal moiré supercell with white dashed lines. The total number of moiré unit cells also follows the $3n^2 - 3n + 1$ rule for the n-th peak. We note that the resonant angles θ_c are almost fixed when changing the width of the bottom nanoribbon as long as the radius of the top circle is kept invariant. Thus we draw a conclusion here that as long as the central TBG region contains one hexagonal moiré supercell (not even a compact one compared to Fig. 5), the resonant tunneling always happens regardless of the shape of the TBG region.

V. SCALING RELATION BETWEEN THE RADIUS R AND THE RESONANT ANGLE θ_c

The period of the moiré pattern of the TBG is defined as the distance between any two adjacent AA stacking regions, or the moiré unit cells, and is calculated to be $L = \sqrt{3}a/(2\sin\theta/2)$. The radius of the circle emcompassing exactly one hexagonal moiré supercell is calculated to be $R_n = \sqrt{S_n}a/(2\sin\theta_{cn}/2)$ for the n-th resonant angle θ_{cn}. To guarantee the full encirclement of the whole hexagonal moiré supercell by the top disk, the radius of the circle in real transport process should be slightly larger than R_n and thus we here consider a modification factor ζ: $R_n \to \zeta R_n$. In Fig. 11, we show the scaling relation of the radius R_n with the n-th resonant angle θ_{cn} in dots read from the numerics. To make a comparison, we also show the theoretically estimated scaling relation $R_n(\theta_{cn})$ with dashed lines. The modification factor ζ has been chosen to be 1.1. A good agreement can be seen between the two methods in Fig. 11, further validating our explanation on the resonant peaks based on the commensuration moiré pattern in TBG.

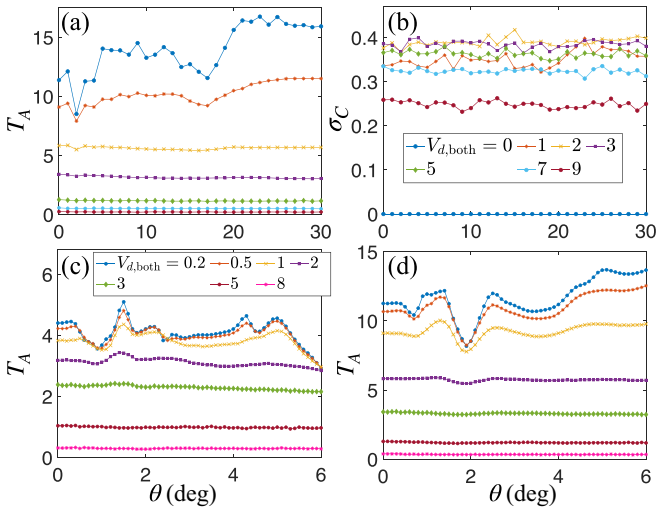

FIG. 12. The calculations with both-layer disorder. [(a) and (b)] The average transmission coefficient T_A, and the conductance fluctuation σ_C (in units of e^2/h) as a function of the rotation angle θ under different disorder strength $V_{d,\text{both}}$. Here the Fermi energy $E_F = 1.2\,\text{eV}$. (a) and (b) share the same legend. [(c) and (d)] The average transmission coefficient T_A as a function of rotation angle θ for $E_F = 0.56$ and 1.2 eV, respectively. For (a)–(d), a disk shape is used, and $N = 50$, $d = a_I$, and $R = W/2$. The disorder is averaged for 1000 times.

VI. DISAPPEARANCE OF COMMENSURATION RESONANCE WITH BOTH-LAYER DISORDER

In this section, we discuss the influence of the bottom-layer disorder on the commensuration resonance. Figure 12 shows the transport calculations through the TBG device with both-layer disorder. Here the central TBG region is still in a disk shape. In Figs. 12(a) and 12(b), the Fermi energy is fixed to $E_F = 1.2\,\text{eV}$, and the average transmission coefficient T_A and the conductance fluctuation σ_C as a function of the rotation angle θ under different disorder strength $V_{d,\text{both}}$ are shown (here the two layers have the same on-site disorder strength). We see that, for weak disorder $V_{d,\text{both}} \leqslant 1\,\text{eV}$, the transmission gets an enhancement after $\theta \geqslant 17^\circ$ as a result of the decoupling regime of the TBG and shows dependence (fluctuation) with the rotation angle. However, after the disorder strength is increased, the angle dependence is smeared out and the average transmission coefficient T_A almost reaches a constant regardless of the rotation angle, consistent with the calculation in Ref. [43]. The conductance fluctuation σ_C also shows no dependence on the rotation angle. Besides, the transmission gets decreased and approaches zero as $V_{d,\text{both}}$ increases, which indicates that strong both-layer disorder tends to localize the electrons inside the TBG region, which is quite different from the top-layer disorder case. For the intermediate disorder strength $2 \leqslant V_{d,\text{both}} \leqslant 5\,\text{eV}$, the conductance fluctuation σ_C is very close to the universal value $0.43e^2/h$ of the 2D mesoscopic conductance fluctuation [76], while for strong disorder σ_C gets decreased as the transport goes into the localization regime. These behaviors all indicate that the transport through a TBG system is quite similar to the normal 2D conductor when both-layer disorder is considered.

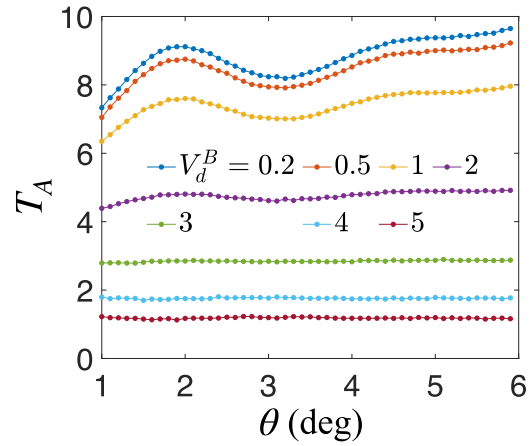

FIG. 13. Average transmission T_A as a function of the rotation angle θ by fixing the top-layer disorder strength $V_d = 5\,\text{eV}$ while varying the bottom-layer disorder strength V_d^B (in units of eV). Here the Fermi energy is $E_F = 1.2\,\text{eV}$. Other parameters are the same as Fig. 12.

To further validate that there is no such commensuration resonance in the both-layer disorder case, in Figs. 12(c) and 12(d) we show the transport results within a small range of rotation angle ($\theta \in [0, 6^\circ]$) by scanning the disorder strength $V_{d,\text{both}}$. We show that, disorder has only two effects on the average transmission coefficient T_A: (1) smears out the fluctuation with respect to the rotation angle and (2) suppresses the transmission. No such resonant peaks are observed in Figs. 12(c) and 12(d) around the two moiré resonant angles θ_{c1} and θ_{c2}.

To indicate how the bottom-layer disorder destroys the resonant phenomenon in detail, in Fig. 13, we adopt a layer-dependent disorder configuration by fixing the top-layer disorder $V_d = 5\,\text{eV}$, and change merely the strength of bottom-layer disorder V_d^B. As can be seen, for weak bottom-layer disorder ($V_d^B \leqslant 2\,\text{eV}$), the resonant peaks can be well kept but with values decreasing as increasing V_d^B. Further increasing V_d^B, the mobility of electrons in the bottom layer is greatly suppressed and electrons tend to be localized (seen from the decreased transmission T_A). The arise of localization in the bottom layer thus totally destroys the resonant phenomenon. The results presented here tell us that one should keep the bottom layer graphene clean or with a high mobility for observing the commensuration resonance reported here.

VII. DISCUSSION AND CONCLUSIONS

The top-layer disorder configuration used in our calculations is crucial for generating the resonant tunneling through the TBG, because the system we are confronting is mesoscopic, where quantum fluctuation as a result of the interference effect would mask the QD effect which exists naturally in 2D moiré systems. Even when the transport system is clean, the TBG region which inherently contains nonuniform interlayer coupling and irregular boundary works as a chaotic system that transmits electrons with random probabilities. Disorder, however, after enough ensemble averages, smears out the fluctuation and finally, unravels the hidden

commensuration effect by exhibiting a resonant tunneling. Here we also want to emphasize that the resonant tunneling due to disorder is newly reported and provides a new perspective into disordered systems.

The robustness of the resonant peak against the disorder strength, the Fermi energy, and the shape distortion of the TBG makes the experimental observation feasible with no requirement for subtle control on those parameters. In addition, in Appendix D, we change the zigzag edge of the graphene nanoribbon into armchair. In Appendix E, we change the on-site Anderson disorder into the long-range disorder. The recurrent resonant peaks at the critical angles in both cases indicate that our commensuration resonant phenomenon does not depend on the graphene nanoribbon edge and the disorder type, either. Our work can find its experimental realization by imitating a similar device in Ref. [77], where a bilayer structure of a rotated hexagonal boron nitride disk on top of a graphene ribbon is demonstrated experimentally. There are two points to be emphasized for experimental detection: (1) one should keep the area of the TBG region invariant upon rotation to avoid other disturbances on the transport and (2) the disorder effect should asymmetrically exists mainly on the top layer. If disorder exists on both layers, the system becomes a trivial 2D disordered conductor which has no such resonant phenomenon (actually a weak disorder is still allowed for the bottom layer, as can be seen in Sec. VI). To make ensemble average, one can change the disorder configuration, or merely fix one configuration by chemical doping or adhering impurities, and then scan the Fermi energy or an external magnetic field (the magnetic field should be small enough to avoid localization or antilocalization effect).

In conclusion, we investigate the quantum transport through a TBG system in a mesoscopic scale, where the TBG system consists of a disordered top layer graphene disk and a clean bottom graphene nanoribboon. We find that with strong disorder, the average transmission through the TBG system shows a sequence of resonant peaks with respect to the rotation angle, with the resonant angles θ_c being robust against the disorder strength, the Fermi energy, and the shape distortion of the central TBG region. We plot the moiré patterns inside the TBG region at the resonant angles and find that the resonance happens when the TBG boundary encompasses one giant hexagonal moiré supercell, and thus has a purely geometric origin. We dub this phenomenon a commensuration resonance and explain it in terms of the QD property of TBG by resembling the resonant tunneling in a conventional mesoscopic QD. Finally the scaling relation of the size of the TBG with respect to the resonant angles θ_c is also given, which shows agreement with the theoretical analysis. The results reported here provide a new way to control the conductance in twisted moiré systems by the rotation angle and should be experimentally observable in a two-terminal mesoscopic system where a nonsymmetric distribution of defects is possible due to adatoms, admolecules, substrate effect or vacancies, etc. [43,78].

ACKNOWLEDGMENTS

We thank L.-W. Fu and W.-L. Zeng for the technical supports on using the Qlab server. We thank X.-C. Xie, J.-H. Gao, and Q.-F. Sun for helpful discussions on the manuscript. The work is supported by the National Science Foundation of China (Grants No. 12204432, No. 12304070), National Key Basic Research Program of China (No. 2020YFB0204800), and Key Research Projects of Zhejiang Lab (No. 2021PB0AC01 and No. 2021PB0AC02).

APPENDIX A: ALGORITHM IN CALCULATING THE TRANSMISSION COEFFICIENTS THROUGH THE TBG SYSTEM

To get the retarded Green's function $\mathbf{G}_C^r$ of the central region numerically as can be seen in Sec. II, we have used an iterative Green's function method. The detailed algorithm can be seen here. (1) Get all the coordinates of all bottom layer within the circle (overlapping region). (2) Rotate the coordinates of all bottom sites within the circle to get the coordinates of all top sites. (3) Sort all the top coordinates of the top layer by ascending x coordinate. (4) Divide the central region into several blocks with length $2\sqrt{3}a$ (see Fig. 14), so that only the nearest blocks have overlapped hopping integrals. (5) Write down the Hamiltonian $\mathbf{H}_i$ of the ith block by calculating the on-site terms and the hopping terms between any two carbon atoms. (6) Write down the hopping matrix $\mathbf{T}_i$ between two adjacent blocks i and $i+1$, and the hopping matrices $\mathbf{T}_{LC}$ and $\mathbf{T}_{CR}$ between the central region and two leads. (7) Use the iterative Green's function method for the one-dimensional prototype [60] to get the Green's function $\mathbf{G}_C^r$.

APPENDIX B: PERIODICITY OF THE TRANSMISSION COEFFICIENT $T(E)$ THROUGH THE TBG REGION

The periodicity of the transmission T or T_A through the TBG region without (with) disorder is shown in Fig. 15. The transmission shows a periodicity of 60° as a result of the circular shape of the central TBG region. The transmission also shows a mirror symmetry about $\theta = \pm 30°$ [see the black dashed lines in Figs. 15(a) and 15(b)] due to the

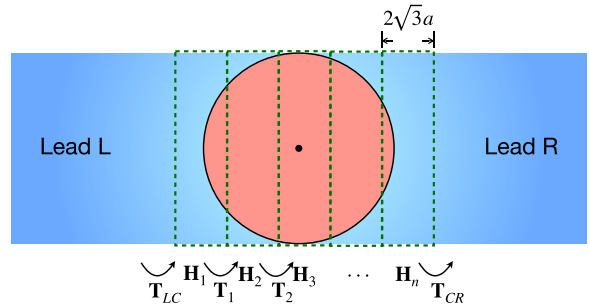

FIG. 14. Schematic diagram of the two-terminal TBG transport system, showing the algorithm of calculating the Green's function $\mathbf{G}_C^r$ of the central region (see the green dashed regions). Here the central region is divided uniformly into several blocks with length $2\sqrt{3}a$. Since we have already set the hopping boundary to be $2\sqrt{3}a$ in the tight-binding model, only the adjacent blocks contribute to nonzero hopping matrices $\mathbf{T}_i$. The matrix for the ith block can be obtained by numerating the coordinates of each carbon atoms within it. The matrices $\mathbf{T}_{LC}$ and $\mathbf{T}_{CR}$ denote the hopping between the central region and the leads L(R).

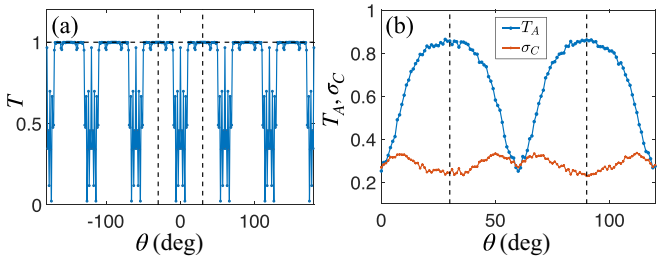

FIG. 15. (a) Transmission coefficient T through the two-terminal TBG system as a function of the rotation angle θ without disorder. The two dashed lines denote the positions of $\theta = \pm 30^\circ$. (b) Average transmission coefficient T_A and conductance fluctuation σ_C as a function of the rotation angle θ. Here the top-layer disorder strength $V_d = 8$ eV. For (a) and (b), the width of the nanoribbon is $N = 50$, the interlayer distance is $d = a_I$, the Fermi energy is $E_F = 0.05$ eV, and the radius of the top disk is $R = W/2$.

mirror symmetry. In addition to the oscillation of the average transmission coefficient T_A in Fig. 15(b), the conductance fluctuation σ_C also has a dependence on θ which has a minimum value at $\theta \approx 30^\circ$ and shows a peak at $\theta \approx 9^\circ$.

APPENDIX C: CONVERGENCE OF THE TRANSMISSION COEFFICIENTS AND CONDUCTANCE FLUCTUATION

To test the convergence of the average transmission T_A and the conductance fluctuation σ_c calculated from a fixed number of ensemble averages, we first plot the T_A curves with respect to the rotation angle θ for the disorder average times $S_d = 1$, 10, 50, 100, 500, 1000 as can be seen in Fig. 16(a). Here we have chosen the TBG region in a disk shape with $R = W/2$. We find that, for one disorder figuration, the resonant peaks can hardly be distinguished due to the strong fluctuation of the transmission as varying θ. After making 10 ensemble averages, the first resonant peak can be distinguished. With increasing the average times, the transmission curves become smoother, and higher resonant peaks can be clearly distinguished. In Fig. 16(b), we choose the rotation angle $\theta = 6^\circ$,

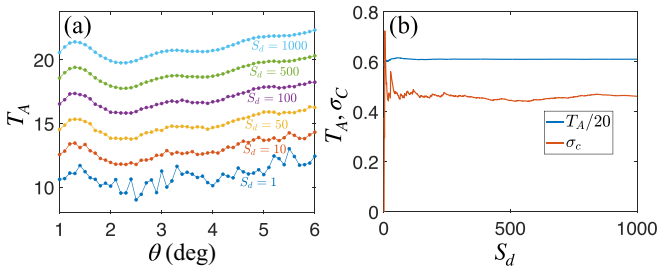

FIG. 16. (a) The average transmission coefficient T_A as a function of the rotation angle θ for different ensemble average times S_d. (b) Convergence of the average transmission coefficient T_A and the conductance fluctuation σ_c at angle $\theta = 6^\circ$ as varying the ensemble average times S_d. Here to show them in the same scale, we have divided T_A by 20. For (a) and (b), we choose $N = 70$, $E_F = 1.2$ eV, $V_d = 5$ eV, $d = a_I$, and $R = W/2$. The disorder exists only on the top layer.

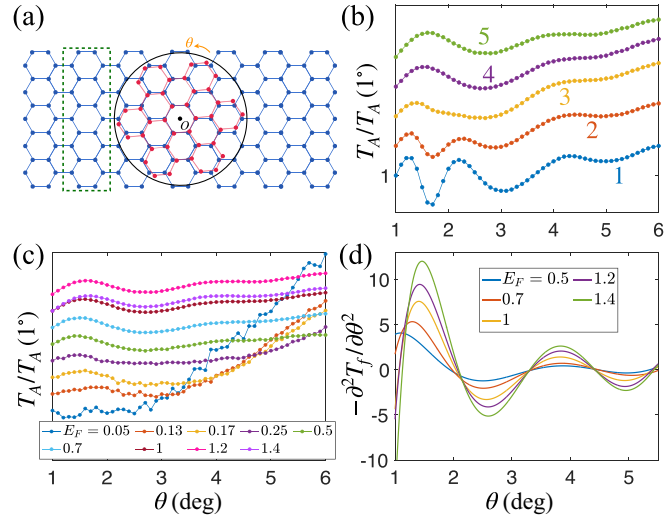

FIG. 17. The calculations with armchair graphene edge. (a) Schematic diagram of TBG device consisting of a bottom graphene nanoribbon with armchair edge and a top graphene disk. Here the rotation center is still chosen at the origin O. The green dashed rectangle labels the unit-block we divided the central region with to calculate the conductance with iterative Green's function method. The width of the bottom nanoribbon is characterized by M which is the number of hexagons along the vertical line crossing O. Here $M = 5$ is shown. (b) Normalized average transmission $T_A/T_A(1^\circ)$ as a function of twist angle θ with different top-layer disorder strength V_d (shown with colored numbers), and with different Fermi energy E_F in (c). (d) The second derivative of the average transmission T_A obtained from the smooth polynomial fitting T_f for (c). For (b)–(d), we used $M = 49$, the radius of the top disk $R = W/2$, and the interlayer distance $d = a_I$. The energy is in units of eV and has been omitted here. The disorder exists only on the top layer and each curve is averaged for 1000 times.

and give the S_d dependence of the average transmission T_A and conductance fluctuation σ_c. Here to show both of them in the same window, we have divided T_A by a factor 20. We see that, the average transmission T_A converges quickly after making 100 ensemble averages. However, the conductance fluctuation converges well only after making around 1000 times of averages. To guarantee the ergodicity of the ensemble, we choose $S_d = 1000$ in all disorder calculations concerning the quantum transport. However, to get the (or to measure) the resonant peaks in the transmission curves, tens of ensemble averages should be enough, which makes the experimental verification of our results quite feasible.

APPENDIX D: COMMENSURATION RESONANCE IN DISORDERED TBG WITH ARMCHAIR EDGE

In the main text, we showed the transport results for the TBG device with zigzag edge along x direction. The zigzag edge features low-energy boundary states as shown in the band structure in Fig. 2(a). However, this kind of boundary states can be eliminated by choosing an armchair edge. In this Appendix, we show the results with an armchair edge. To do this we first consider the transport device shown in Fig. 17(a), which has similar structure as Fig. 1. The rotational

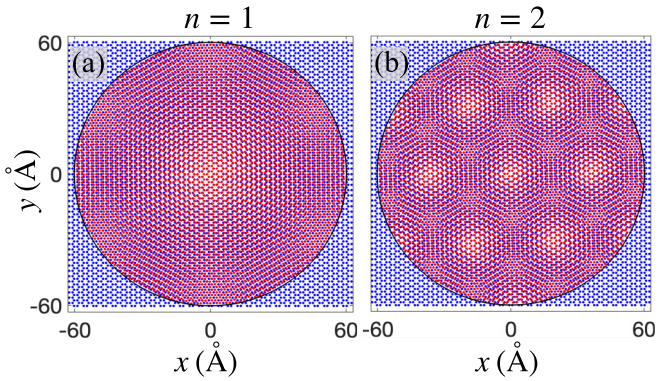

FIG. 18. The moiré pattern plotted for the first resonant angle $\theta_{c1} = 1.42^\circ$ in (a), and the second resonant angle $\theta_{c2} = 3.84^\circ$ in (b) for the TBG device with armchair edge. Here the width of the bottom nanoribbon is $M = 49$. The critical angles θ_c were read out from the second derivative of the conductance curve at $E_F = 1.2\,\text{eV}$ in Fig. 17(d).

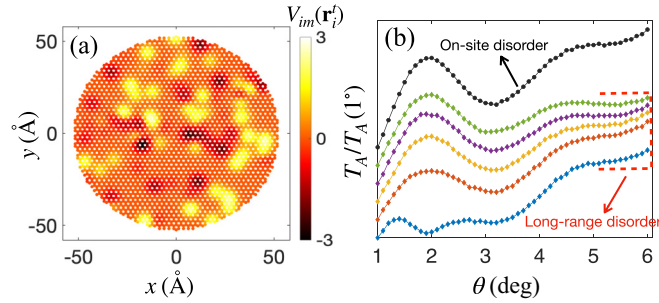

FIG. 19. (a) Landscape of long-range disorder potential $V_{im}(\mathbf{r}_i^t)$ generated by 100 impurities randomly distributed on the top graphene disk. The correlation length of the impurity $\xi = 2a$, and the top-layer disorder strength is chosen $V_d = 5\,\text{eV}$. The width of the bottom nanoribbon with zigzag edge is $N = 50$, and the twist angle $\theta = 0$. Only one disorder configuration is shown here. (b) Normalized average transmission $T_A/T_A(1^\circ)$ as a function of the twist angle θ with different number of impurities $\mathcal{N}_{im}$, shown with colored diamond (embraced by the dashed line). From blue to green the number of impurities is: 50, 100, 150, 200, and 250. For comparison, the result of applying the on-site disorder is also shown here (see the black dotted curve). For both on-site and long-range disorder the disorder strength V_d is chosen at 5 eV.

center is still chosen at the origin O which is the center of the bottom hexagon. The radius of the top disk is $R = W/2$ with the width of the bottom nanoribbon $W = M\sqrt{3}a$, where M is the number of hexagons along the vertical line crossing O. In Fig. 17(a), an $M = 5$ is shown. In the following descriptions, we will use M to characterize the width of the bottom nanoribbon. In calculating the two-terminal conductance using the iterative Green's function method, we have divided the central region uniformly into several blocks [shown within the green dashed rectangle in Fig. 17(a)] with length $3a$. So we have set the hopping range to be $3a$ in the tight-binding calculations for numerical feasibility. In Fig. 17(b), we show the average transmission coefficient T_A [normalized by $T_A(1^\circ)$] varying with the rotation angle θ with different top-layer disorder strength V_d. As shown clearly, for weak disorder strength, the average transmission curve shows strong fluctuation as varying θ. With increasing the disorder strength, the fluctuations are smeared out, and two universal conductance peaks can be resolved. Figure 17(c) shows the Fermi energy E_F dependence of the average transmission coefficient T_A by fixing the top-layer disorder strength $V_d = 5\,\text{eV}$. For small Fermi energy, which is quite close to the Dirac point, there is only one incident mode transmitting through the central TBG region due to the finite-size effect, and the resonant peaks can not be observed. However, as the Fermi energy is lifted and the incident number of modes increases, the $n = 1$ resonant peak first arises. With further increasing E_F, the position of the first resonant peak is almost fixed and the second resonant peak arises. Figure 17(d) indicates the second derivative of the resonant curves for high Fermi energies and gives the first resonant angle $\theta_{c1} = 1.42^\circ$ and the second resonant angle $\theta_{c2} = 3.84^\circ$ (read from $E_F = 1.2\,\text{eV}$). In Figs. 18(a) and 18(b), we plot the moiré pattern for $\theta = \theta_{c1}$ and θ_{c2}, respectively. The disk enclosing one whole hexagonal moiré supercell, which can be fractionalized into one and seven moiré unit cells, with the boundary of the disk crossing the AB/BA stacking regions, indicates the same commensuration resonant phenomenon for TBG with armchair edge.

APPENDIX E: COMMENSURATION RESONANCE WITH LONG-RANGE DISORDER ON THE TOP LAYER

In the main text and the appendices before, we used the on-site Anderson-type disorder which is short-ranged in the atomic scale. To show that the commensuration resonance is universal regardless of the disorder type, we replace the Anderson disorder with a long-range disorder potential by changing ε_i into $\varepsilon_i = \varepsilon_0 + V_{im}(\mathbf{r}_i^t)$. Still the disorder potential exists only on the top layer, and can be generated by $\mathcal{N}_{im}$ impurities centered at $\mathbf{r}_m^t$, randomly distributed among the top layer atomic sites $\{\mathbf{r}_i^t\}$. The impurity potential takes the form: $V_{im}(\mathbf{r}_i^t) = \sum_{m=1}^{\mathcal{N}_{im}} U_m \exp[-|\mathbf{r}_i^t - \mathbf{r}_m^t|^2/(2\xi^2)]$, where ξ denotes the correlation length of the impurity, and U_m characterizing the strength of the m-th impurity is uniformly distributed within $[-V_d/2, V_d/2]$. In the following calculations we use $\xi = 2a$ and the disorder strength $V_d = 5\,\text{eV}$. This set of parameters can well simulate a realistic disordered graphene with long-range impurities, and has been widely used in Refs. [79–82].

In Fig. 19(a), we show the landscape of one configuration of the long-range disorder potential. Here a zigzag graphene edge is used. The number of impurities is set to $\mathcal{N}_{im} = 100$, and considering the top-layer atom number $\mathcal{N}_{\text{top}} = 3306$, the density of impurities $n_I \equiv \mathcal{N}_{im}/\mathcal{N}_{\text{top}} \approx 3\%$. In Fig. 19(b), we show the transport results in the presence of long-range impurities. For comparison, the result with on-site disorder is also shown (see black dotted curve). The disorder strength V_d is chosen at 5 eV. As can be seen, for low impurity density ($\mathcal{N}_{im} = 50$), the first commensuration resonant peak is absent due to the strong fluctuation of T_A as varying θ while the second peak can be observed. Further increasing the impurity density, both peaks can be seen very clearly. Besides, the first resonant peak is almost pinned at the same position as the on-site case. The shift of the second peak is due to the

change of the global slope of the curve around the second resonant angle, in the same origin as the peak shift in Fig. 4(a). The results presented here indicate the same commensuration resonant phenomenon in the long-range disorder case.

[1] Y. Cao, V. Fatemi, S. Fang, K. Watanabe, T. Taniguchi, E. Kaxiras, and P. Jarillo-Herrero, Unconventional superconductivity in magic-angle graphene superlattices, Nature (London) **556**, 43 (2018).

[2] Y. Cao *et al.*, Correlated insulator behaviour at half-filling in magic-angle graphene superlattices, Nature (London) **556**, 80 (2018).

[3] D. Wong, K. P. Nuckolls, M. Oh, B. Lian, Y. Xie, S. Jeon, K. Watanabe, T. Taniguchi, B. A. Bernevig, and A. Yazdani, Cascade of electronic transitions in magic-angle twisted bilayer graphene, Nature **582**, 198 (2020).

[4] E. Y. Andrei and A. H. MacDonald, Graphene bilayers with a twist, Nat. Mater. **19**, 1265 (2020).

[5] J. Y. Lee, E. Khalaf, S. Liu, X. Liu, Z. Hao, P. Kim, and A. Vishwanath, Theory of correlated insulating behaviour and spin-triplet superconductivity in twisted double bilayer graphene, Nat. Commun. **10**, 5333 (2019).

[6] L. Balents, C. R. Dean, D. K. Efetov, and A. F. Young, Superconductivity and strong correlations in moiré flat bands, Nat. Phys. **16**, 725 (2020).

[7] D. M. Kennes, J. Lischner, and C. Karrasch, Strong correlations and $d + id$ superconductivity in twisted bilayer graphene, Phys. Rev. B **98**, 241407(R) (2018).

[8] F. Wu, and S. Das Sarma, Identification of superconducting pairiing symmetry in twisted bilayer graphene using in-plane magnetic field and strain, Phys. Rev. B **99**, 220507(R) (2019).

[9] X. Gu, C. Chen, J. N. Leaw, E. Laksono, V. M. Pereira, G. Vignale, and S. Adam, Antiferromagnetism and chiral d-wave superconductivity from an effective $t - J - D$ model for twisted bilayer graphene, Phys. Rev. B **101**, 180506(R) (2020).

[10] A. Fischer, L. Klebl, C. Honerkamp, and D. M. Kennes, Spin-fluctuation-induced pairing in twisted bilayer graphene, Phys. Rev. B **103**, L041103 (2021).

[11] C.-C. Liu, L.-D. Zhang, W.-Q. Chen, and F. Yang, Chiral spin density and $d + id$ superconductivity in the magic-angle-twisted bilayer graphene, Phys. Rev. Lett. **121**, 217001 (2018).

[12] J. M. B. Lopes dos Santos, N. M. R. Peres, and A. H. Castro Neto, Graphene bilayer with a twist: Electronic structure, Phys. Rev. Lett. **99**, 256802 (2007).

[13] R. Bistritzer and A. H. MacDonald, Moiré bands in twisted double-layer graphene, Proc. Natl. Acad. Sci. USA **108**, 12233 (2011).

[14] J. M. B. Lopes dos Santos, N. M. R. Peres, and A. H. Castro Neto, Continuum model of the twisted graphene bilayer, Phys. Rev. B **86**, 155449 (2012).

[15] E. Suárez Morell, J. D. Correa, P. Vargas, M. Pacheco, and Z. Barticevic, Flat bands in slightly twisted bilayer graphene: Tight-binding calculations, Phys. Rev. B **82**, 121407(R) (2010).

[16] A. L. Sharpe, E. J. Fox, A. W. Barnard, J. Finney, K. Watanabe, T. Taniguchi, M. A. Kastner, and D. Goldhaber-Gordon, Emergent ferromagnetism near three-quarters filling in twisted bilayer graphene, Science **365**, 605 (2019).

[17] J.-X. Lin, Y.-H. Zhang, E. Morissette, Z. Wang, S. Liu, D. Rhodes, K. Watanabe, T. Taniguchi, J. Hone, and J. I. A. Li, Spin-orbit-driven ferromagnetism at half moiré filling iin magic-angle twisted bilayer graphene, Science **375**, 437 (2022).

[18] Y. Zhang, Z. Hou, Y.-X. Zhao, Z.-H. Guo, Y.-W. Liu, S.-Y. Li, Y.-N. Ren, Q.-F. Sun, and L. He, Correlation-induced valley splitting and orbital magnetism in a strain-induced zero-energy flatband in twisted bilayer graphene near the magic angle, Phys. Rev. B **102**, 081403(R) (2020).

[19] Y. Saito, J. Ge, L. Rademaker, K. Watanabe, T. Taniguchi, D. A. Abanin, and A. F. Young, Hofstadter subband ferromagnetism and symmetry-broken Chern insulators in twisted bilayer graphene, Nat. Phys. **17**, 478 (2021).

[20] M. Serlin, C. L. Tschirhart, H. Polshyn, Y. Zhang, J. Zhu, K. Watanabe, T. Taniguchi, L. Balents, and A. F. Young, Intrinsic quantized anomalous Hall effect in a moiré heterostructure, Science **367**, 900 (2020).

[21] S. Wu, Z. Zhang, K. Watanabe, T. Taniguchi, and E. Y. Andrei, Chern insulators, van Hove singularities and topological flat bands in magic-angle twisted bilayer graphene, Nat. Mater. **20**, 488 (2021).

[22] P. Stepanov *et al.*, Untying the insulating and superconducting orders in magic-angle graphene, Nature (London) **583**, 375 (2020).

[23] M. Christos, S. Sachdev, and M. S. Scheurer, Correlated insulators, semimetals, and superconductivity in twisted trilayer graphene, Phys. Rev. X **12**, 021018 (2022).

[24] S. Chen, M. He, Y.-H. Zhang, V. Hsieh, Z. Fei, K. Watanabe, T. Taniguchi, D. H. Cobden, X. Xu, C. R. Dean, and M. Yankowitz, Electrically tunable correlated and topological states in twisted monolayer-bilayer graphene, Nat. Phys. **17**, 374 (2021).

[25] Z. Ma, S. Li, Y.-W. Zheng, M.-M. Xiao, H. Jiang, J.-H. Gao, and X. C. Xie, Topological flat bands in twisted trilayer graphene, Sci. Bull. **66**, 18 (2021).

[26] Z. Ma, S. Li, M. Lu, D.-H. Xu, J.-H. Gao, and X. C. Xie, Doubled moiré flat bands in double-twisted few-layer graphite, Sci. China Phys. Mech. Astron. **66**, 227211 (2023).

[27] D. Călugáru, F. Xie, Z.-D. Song, B. Lian, N. Regnault, and B. A. Bernevig, Twisted symmetric trilayer graphene: Single-particle and many-body Hamiltonians and hidden nonlocal symmetries of trilayer moiré systems with and without displacement field, Phys. Rev. B **103**, 195411 (2021).

[28] F. Xie, N. Regnault, D. Călugáru, B. A. Bernevig, and B. Lian, Twisted symmetric trilayer graphene. II. Projected Hartree-Fock study, Phys. Rev. B **104**, 115167 (2021).

[29] Y. Cao, D. Rodan-Legrain, O. Rubies-Bigorda, J. M. Park, K. Watanabe, T. Taniguchi, and P. Jarillo-Herrero, Tunable correlated states and spin-polarized phases in twisted bilayer-bilayer graphene, Nature (London) **583**, 215 (2020).

[30] M. Lu, J. Zeng, H. Liu, J.-H. Gao, and X. C. Xie, Valley-selective Floquet Chern flat bands in twisted multilayer graphene, Phys. Rev. B **103**, 195146 (2021).

[31] M. Chen, X. Lin, T. H. Dinh, Z. Zheng, J. Shen, Q. Ma, H. Chen, P. Jarillo-Herrero, and S. Dai, Configurable phonon polaritons in twisted α-MoO_3, Nat. Mater. **19**, 1307 (2020).

[32] L. Wang *et al.*, Correlated electronic phases in twisted bilayer transition metal dichalcogenides, Nat. Mater. **19**, 861 (2020).

[33] D. M. Kennes, M. Claassen, L. Xian, A. Georges, A. J. Millis, J. Hone, C. R. Dean, D. N. Basov, A. N. Pasupathy, and A. Rubio, Moiré heterostructures as a condensed-matter quantum simulator, Nat. Phys. **17**, 155 (2021).

[34] D. A. Bahamon, G. Gómez-Santos, and T. Stauber, Emergent magnetic texture in driven twisted bilayer graphene, Nanoscale **12**, 15383 (2020).

[35] S. G. de Castro, A. Ferreira, and D. A. Bahamon, Efficient Chebyshev polynomial approach to quantum conductance calculations: Application to twisted bilayer graphene, Phys. Rev. B **107**, 045418 (2023).

[36] D. A. Bahamon, G. Gómez-Santos, D. K. Efetov, and T. Stauber, Chirality probe of twisted bilayer graphene in the linear transport regime, arXiv:2307.03779 v1.

[37] E. Suarez Morell, R. Vergara, M. Pacheco, L. Brey, and L. Chico, Electronic properties of twisted bilayer nanoribbons, Phys. Rev. B **89**, 205405 (2014).

[38] E. S. Morell, P. Vargas, P. Häberle, S. A. Hevia, and L. Chico, Edge states of moiré structures in graphite, Phys. Rev. B **91**, 035441 (2015).

[39] M. Pelc, E. Suárez Morell, L. Brey, and L. Chico, Electronic Conductance of Twisted Bilayer Nanoribbon Flakes, J. Phys. Chem. C **119**, 10076 (2015).

[40] Y. Han, J. Zeng, Y. Ren, X. Dong, W. Ren, and Z. Qiao, Mesoscopic electronic transport in twisted bilayer graphene, Phys. Rev. B **101**, 235432 (2020).

[41] H. Z. Olyaei, B. Amorim, P. Ribeiro, and E. V. Castro, Ballistic charge transport in twisted bilayer graphene, arXiv:2007.14498 v1.

[42] C. De Beule, P. G. Silvestrov, M.-H. Liu, and P. Recher, Valley splitter and transverse valley focusing in twisted bilayer graphene, Phys. Rev. Res. **2**, 043151 (2020).

[43] O. F. Namarvar, A. Missaoui, L. Magaud, D. Mayou, and G. Trambly de Laissardière, Electronic structure and quantum transport in twisted bilayer graphene with resonant scatterers, Phys. Rev. B **101**, 245407 (2020).

[44] M. Alvarado and A. L. Yeyati, Transport and spectral properties of magic-angle twisted bilayer graphene junctions based on local orbital models, Phys. Rev. B **104**, 075406 (2021).

[45] M. Anđelković, L. Covaci, and F. M. Peeters, DC conductivity of twisted bilayer graphene: Angle-dependent transport properties and effects of disorder, Phys. Rev. Mater. **2**, 034004 (2018).

[46] X. Ye, H. Xu, and X. Zhu, Floquet electronic bands and transport in magic-angle bilayer graphene, New J. Phys. **24**, 063029 (2022).

[47] A. Sanjuan Ciepielewski, J. Tworzydło, T. Hyart, and A. Lau, Transport signatures of Van Hove singularities in mesoscopic twisted bilayer graphene, Phys. Rev. Res. **4**, 043145 (2022).

[48] G. Sharma, I. Yudhistira, N. Chakraborty, D. Y. H. Ho, M. M. Al Ezzi, M. S. Fuhrer, G. Vignale, and S. Adam, Carrier transport theory for twisted bilayer graphene in the metallic regime, Nat. Commun. **12**, 5737 (2021).

[49] G. Trambly de Laissardière, D. Mayou, and L. Magaud, Localization of dirac electrons in rotated graphene bilayers, Nano Lett. **10**, 804 (2010).

[50] G. Trambly de Laissardière, D. Mayou, and L. Magaud, Numerical studies of confined states in rotated bilayers of graphene, Phys. Rev. B **86**, 125413 (2012).

[51] V. N. Do, H. A. Le, and D. Bercioux, Time-evolution of electrons in twisted bilayer graphene, Phys. Rev. B **99**, 165127 (2019).

[52] G. Li, A. Luican, J. M. B. Lopes dos Santos, A. H. Castro Neto, A. Reina, J. Kong, and E. Y. Andrei, Observation of Van Hove singularities in twisted graphene layers, Nat. Phys. **6**, 109 (2010).

[53] A. Luican, G. Li, A. Reina, J. Kong, R. R. Nair, K. S. Novoselov, A. K. Geim, and E. Y. Andrei, Single-layer behavior and its breakdown in twisted graphene layers, Phys. Rev. Lett. **106**, 126802 (2011).

[54] I. Brihuega, P. Mallet *et al.*, Unraveling the intrinsic and robust nature of van hove sigularities in twisted bilayer graphene by scanning tunneling microscopy and theoretical analysis, Phys. Rev. Lett. **109**, 196802 (2012).

[55] L.-J. Yin, J.-B. Qiao, W.-J. Zuo, W.-T. Li, and L. He, Experimental evidence for non-Abelian gauge potentials in twisted graphene bilayers, Phys. Rev. B **92**, 081406(R) (2015).

[56] A. Nimbalkar and H. Kim, Opportunities and challenges in twisted bilayer graphene: A review, Nano-Micro Lett. **12**, 126 (2020).

[57] J. C. Slater and G. F. Koster, Simplified LCAO method for the periodic potential problem, Phys. Rev. **94**, 1498 (1954).

[58] M. Mirzakhani, F. M. Peeters, and M. Zarenia, Circular quantum dots in twisted bilayer graphene, Phys. Rev. B **101**, 075413 (2020).

[59] M. P. Lopez Sancho, J. M. Lopez Sancho, J. M. L. Sancho, and J. Rubio, Highly convergent schemes for the calculation of bulk and surface Green functions, J. Phys. F: Met. Phys. **15**, 851 (1985).

[60] V.-N. Do, Non-equilibrium green function method: Theory and application in simulation of nanometer electronic de- vices, Adv. Nat. Sci.: Nanosci. Nanotechnol. **5**, 033001 (2014).

[61] S. Datta, *Electronic Transport in Mesoscopic Systems* (Cambridge University Press, Cambridge, 1995), pp. 133–136.

[62] Y. Meir and N. S. Wingreen, Landauer formula for the current through an interacting electron region, Phys. Rev. Lett. **68**, 2512 (1992).

[63] A.-P. Jauho, N. S. Wingreen, and Y. Meir, Time-dependent transport in interacting and noninteracting resonant-tunneling systems, Phys. Rev. B **50**, 5528 (1994).

[64] S. Ryu and Y. Hatsugai, Topological origin of zero-energy edge states in particle-hole symmetric systems, Phys. Rev. Lett. **89**, 077002 (2002).

[65] G. C. Paul, P. Recher, and L. Santos, Particle dynamics and ergodicity-breaking in twisted-bilayer optical lattices, arXiv:2306.01588 v1.

[66] X. R. Wang, Y. Wang, and Z. Z. Sun, Antiresonance scattering at defect levels in the quantum conductance of a one-dimensional system, Phys. Rev. B **65**, 193402 (2002).

[67] J. A. Crosse and P. Moon, Quasicrystalline electronic states in twisted bilayers and the effects of interlayer and sublattice symmetries, Phys. Rev. B **103**, 045408 (2021).

[68] Y. Fukaya, Y. Zhao, H.-W. Kim, J. R. Ahn, H. Fukidome, and I. Matsuda, Atomic arrangements of quasicrystal bilayer graphene: Interlayer distance expansion, Phys. Rev. B **104**, L180202 (2021).

[69] B. Deng, B. Wang, N. Li, R. Li, Y. Wang, J. Tang, Q. Fu, Z. Tian, P. Gao, J. Xue, and H. Peng, Interlayer decoupling in 30° twisted bilayer graphene quasicrystal, ACS Nano **14**, 1656 (2020).

[70] J. Berashevich and T. Chakraborty, Interlayer repulsion and decoupling effects in stacked turbostratic graphene flakes, Phys. Rev. B **84**, 033403 (2011).

[71] J. Hass *et al.*, Why multilayer graphene on 4H-SiC(000$\bar{1}$) behaves like a single sheet of graphene, Phys. Rev. Lett. **100**, 125504 (2008).

[72] The localization length λ_L is determined by calculating the limit: $-2\lim_{L\to\infty} L/(\ln T_A)$ where T_A is the average transmission coefficient through a disordered graphene nanoribbon with length L using the recursive Green's function method.

[73] The higher Fermi level crosses more transmission channels from the leads so that the density of states within the TBG region become more, and as a result, the resonant transmission mediated by the quantum dot structure can be enhanced.

[74] M. Yankowitz, J. Jung, E. Laksono, N. Leconte, B. L. Chittari, K. Watanabe, T. Taniguchi, S. Adam, D. Graf, and C. R. Dean, Dynamic band-structure tuning of graphene moiré superlattices with pressure, Nature (London) **557**, 404 (2018).

[75] B. Padhi and P. W. Phillips, Pressure-induced metal-insulator transition in twisted bilayer graphene, Phys. Rev. B **99**, 205141 (2019).

[76] Y. Hu, H. Liu, H. Jiang, and X. C. Xie, Numerical study of universal conductance fluctuations in three-dimensional topological semimetals, Phys. Rev. B **96**, 134201 (2017).

[77] R. Ribeiro-Palau, C. Zhang, K. Watanabe, T. Taniguchi, J. Hone, and C. R. Dean, Twistable electronics with dynamically rotatable heterostructures, Science **361**, 690 (2018).

[78] P. Moles, F. Domínguez-Adame, and L. Chico, Impact of vacancies on twisted bilayer graphene quantum point contacts, arXiv:2307.06819 v1.

[79] Y.-Y. Zhang, J. Hu, B. A. Bernevig, X. R. Wang, X. C. Xie, and W. M. Liu, Localization and the kosterlitz-thouless transition in disordered graphene, Phys. Rev. Lett. **102**, 106401 (2009).

[80] L. P. Zârbo and B. K. Nikolić, Spatial distribution of local currents of massless Dirac fermions in quantum transport through graphene nanoribbons, Europhys. Lett. **80**, 47001 (2007).

[81] C. H. Lewenkopf, E. R. Mucciolo, and A. H. Castro Neto, Numerical studies of conductivity and Fano factor in disordered graphene, Phys. Rev. B **77**, 081410(R) (2008).

[82] K. Wakabayashi, Y. Takane, and M. Sigrist, Perfectly conducting channel and universality crossover in disordered graphene nanoribbons, Phys. Rev. Lett. **99**, 036601 (2007).